Results in Engineering 31 (2026) 111507

Contents lists available at ScienceDirect

Results in Engineering

journal homepage: www.sciencedirect.com/journal/results-in-engineering

Research paper

Carbon nanostructure interlayer-driven charge transfer engineering in lead-free $CsSnCl_3$ perovskite photovoltaics

Ghodrat Mahmoudi [a,b], Masood Mehrabian [c,*], Pourya Norouzzadeh [d], Maryam Taleb-Abbasi [e], Asmet N. Azizova [f,g,h], Sonya Aslyousefzadeh [c], Omid Akhavan [i,*]

[a] Department of Chemistry, Faculty of Science, University of Maragheh, P.O. Box 55136-83111, Maragheh, Iran
[b] Department of Chemistry, Dogus University, Dudullu-Ümraniye, 34775 Istanbul, Türkiye
[c] Department of Physics, Faculty of Basic Science, University of Maragheh, P.O. Box 55181-83111, Maragheh, Iran
[d] Department of Physics, Faculty of Sciences, Urmia University, Urmia, Iran
[e] Department of Physical Chemistry, Faculty of Chemistry, University of Tabriz, Tabriz, Iran
[f] Scientific Research Center, Baku Engineering University, Hasan Aliyev str. 120, AZ0101, Khirdalan, Absheron, Azerbaijan
[g] Azerbaijan Medical University, Scientific Research Centre (SRC), A. Kasumzade, St. 14. AZ 1022, Baku, Azerbaijan
[h] Western Caspian University, Istiqlaliyyat Street 31, AZ 1001, Baku, Azerbaijan
[i] Department of Physics, Sharif University of Technology, P.O. Box 11155-9161, Tehran, Islamic Republic of Iran

ARTICLE INFO

Keywords:
$CsSnCl_3$ perovskite
Pb-free solar cells
Carbon nanomaterials
C_{60}
SWCNT
TiO_2 electron transport layer
Nyquist analysis

ABSTRACT

This simulation-based study investigates the influence of carbon-based interlayers on the theoretically predicted performance of $CsSnCl_3$ perovskite solar cells by incorporating C_{60} and single-wall carbon nanotubes (SWCNTs) between TiO_2 and the absorber. All results reported herein are obtained from numerical simulations using SCAPS-1D and represent theoretical upper bounds under idealized, defect-minimized conditions. It is important to note that the assumed $CsSnCl_3$ bandgap of 1.52 eV is a hypothetical, strain-tuned value; experimentally synthesized $CsSnCl_3$ typically exhibits a bandgap of approximately 2.8 eV. Therefore, this study should be interpreted as a design exploration for future bandgap engineering efforts, not as a prediction of currently achievable experimental performance. Device simulations reveal that the TiO_2-only structure exhibits the highest charge transfer resistance and lowest built-in potential, resulting in moderate efficiency. Introducing C_{60} improves interfacial band alignment and increases both the open circuit voltage and built-in potential, yielding a notable enhancement in power conversion efficiency. The most significant improvement is achieved with SWCNTs, which substantially reduce the charge transfer resistance and facilitate more efficient electron extraction. This leads to a marked increment in the highest overall efficiency and short circuit current density among the studied architectures. Nyquist analysis confirms the correlation between reduced impedance, improved interfacial charge transfer, and enhanced photovoltaic performance. These findings highlight the effectiveness of SWCNTs as an interfacial layer for optimizing charge transport and maximizing the theoretically predicted performance of lead-free perovskite solar cells under idealized conditions.

1. Introduction

Perovskite solar cells (PSCs) have become one of the most exciting technologies in renewable energy because they can reach high efficiency with relatively simple fabrication. However, most high-performance PSCs are based on lead halide perovskites, and the presence of toxic lead raises serious environmental and health concerns [1,2].

This has motivated researchers to explore lead-free alternatives, especially germanium [3,4] and tin-based perovskites [5,6]. Among them, $CsSnCl_3$ has attracted attention due to its suitable bandgap, strong optical absorption, and potential for stable operation without lead [7,8].

Even though $CsSnCl_3$ is promising, tin-based perovskites often face challenges such as high defect density, poor charge transport, and recombination losses. These problems reduce efficiency compared to lead-based devices. One effective way to address these issues is to improve the interfaces between the absorber and the electron transport layer (ETL). TiO_2 is commonly used as the ETL, but mismatched energy levels and interfacial defects can increase charge transfer resistance and

* Corresponding authors.
E-mail addresses: masood.mehrabian@maragheh.ac.ir (M. Mehrabian), oakhavan@sharif.edu (O. Akhavan).

https://doi.org/10.1016/j.rineng.2026.111507
Received 27 February 2026; Received in revised form 8 June 2026; Accepted 10 June 2026
Available online 16 June 2026

limit performance [9,10].

To overcome these limitations, researchers have introduced carbon nanostructures as interlayers between TiO_2 and the perovskite absorber. Materials such as fullerene (C_{60}) and single-walled carbon nanotubes (SWCNTs) are widely studied because of their excellent conductivity, stability, and ability to align energy levels [11].

While carbon interlayers have been explored in lead-based and some lead-free perovskite systems, their specific role in $CsSnCl_3$ — a material whose experimental bandgap (~2.8 eV) differs significantly from the value often assumed in simulations (1.52 eV under specific lattice strain) — remains poorly understood. While graphene and reduced graphene oxide (rGO) have also shown promise as interfacial layers [12], the present work focuses on C_{60} and SWCNTs as representative 0D and 1D carbon nanostructures to compare discrete molecular versus network-based charge extraction. Systematic comparison with graphene-based interlayers is left for future study.

This study does not aim to claim record efficiencies for experimentally realistic $CsSnCl_3$, but rather to explore the theoretical potential of bandgap-tuned $CsSnCl_3$ (e.g., via strain or alloying) when combined with carbon interlayers. The key novelty lies in the comparative analysis of C_{60} vs. SWCNT interlayers specifically for a 1.52 eV $CsSnCl_3$ absorber, providing design guidelines for future experimental efforts to tune the bandgap of this material toward the Shockley-Queisser optimum [13].

Recent studies on multi-layered perovskite light harvesters have demonstrated the benefits of optimized charge transport layers [14,15].

Fullerene derivatives like C_{60} and PCBM have been shown to improve band alignment and reduce recombination in perovskite devices [16,17]. SWCNTs, on the other hand, provide highly conductive pathways for electron transport and have been successfully used in flexible optoelectronic devices [18,19].

Electrochemical impedance spectroscopy (EIS), especially Nyquist analysis, is a powerful tool to study these effects [20]. Nyquist plots reveal how interfacial resistance changes with different interlayers. Devices with carbon nanostructures often show smaller semicircles in Nyquist plots, which means lower resistance and faster charge transfer. Several studies confirm that impedance spectroscopy can directly link reduced resistance to improved efficiency and stability in PSCs [2,21–26].

Recent SCAPS-1D studies on interface engineering in perovskite solar cells have highlighted the importance of defect passivation and band alignment optimization [27,28].

In this work, we investigate $CsSnCl_3$ solar cells modified with carbon nanostructure interlayers. Three device architectures are compared: TiO_2 only, TiO_2/C_{60}, and TiO_2/SWCNT. The TiO_2-only device shows high resistance and moderate efficiency. Adding C_{60} improves voltage output by better band alignment, but resistance remains relatively high. The most significant improvement comes from SWCNTs, which strongly reduce charge transfer resistance and enable efficient electron extraction. Nyquist analysis confirms these findings, with the SWCNT device showing the smallest semicircle and the best charge transport.

By combining a lead-free absorber with conductive carbon nanostructures, this study demonstrates a practical pathway to improve efficiency and stability in tin-based perovskite solar cells. The results highlight the importance of interfacial engineering and suggest that carbon nanostructures, especially SWCNTs, can play a key role in advancing the next generation of environmentally friendly PSCs.

2. Important note on $CsSnCl_3$ bandgap

The present study assumes a $CsSnCl_3$ bandgap of 1.52 eV, following previous simulation works [9]. However, it is important to acknowledge that experimentally synthesized $CsSnCl_3$ typically exhibits a much wider bandgap of approximately 2.8–3.0 eV under ambient conditions. The 1.52 eV value has been primarily reported in density functional theory (DFT) calculations under specific lattice parameters or strained conditions [7,8]. Experimental realization of a 1.52 eV $CsSnCl_3$ would likely require significant bandgap engineering (e.g., alloying, strain, or quantum confinement). Therefore, the high efficiencies reported herein (up to 28%) represent theoretical upper bounds for a hypothetical bandgap-tuned $CsSnCl_3$ absorber, not predictions for currently achievable experimental devices. This study should be interpreted as a design exploration for future bandgap engineering efforts, not as a claim of near-term experimental feasibility.

3. Device structure and simulation

The **SCAPS-1D simulator (**Solar Cell Capacitance Simulator) is employed as the primary computational tool for modeling and analyzing the optoelectronic behavior of thin-film perovskite solar cells (PSCs) [29,30]. Developed by the Department of Electronics and Information Systems at the University of Ghent, Belgium [31–33], SCAPS is an open source platform that numerically solves drift–diffusion transport equations, the hole and electron continuity equations, and Poisson's equation. Together, these form the core framework for describing charge generation, transport, and recombination within multilayer photovoltaic structures.

4. Model calibration and benchmarking

We benchmarked our SCAPS-1D model by simulating an experimentally validated $MAPbI_3$ device (FTO/ZnO/$MAPbI_3$/Cu_2O/Au) using parameters from Mehrabian et al. [6]. Our simulation reproduced the reported PCE of 6.06%, matching the experimental ~6% value (difference <1%), confirming the physical validity of our parameter choices. For $CsSnCl_3$ with the hypothetical 1.52 eV bandgap, no experimental device exists for direct validation. Therefore, we adopted defect-minimized parameters from Hossain et al. [9] (originally calibrated for ~2.8 eV $CsSnCl_3$) and explicitly state that our results (up to 28% PCE) represent theoretical upper bounds under idealized, interface-defect-free conditions.

5. Limitations of the SCAPS-1D model for tin perovskites

SCAPS-1D is a drift-diffusion solver that assumes fixed ion positions and does not explicitly model trap-state migration. However, tin-based perovskites are known to exhibit mobile ions (e.g., vacancies, interstitial Sn^{2+}) that can influence charge transfer resistance and impedance response, particularly at low frequencies. The absence of trap-state migration in our model means that the simulated EIS response (Fig. 5) may not fully capture real-world behavior. Future work should employ models that couple electronic and trap-state transport (e.g., drift-diffusion with trap-state rate equations) to more accurately simulate frequency-dependent ionic-electronic coupling. The present results should therefore be interpreted as electronic-only transport predictions.

As an initial step, a device with the configuration **FTO/TiO_2/$CsSnCl_3$/PEDOT:PSS/Ag** was simulated. Band alignment plays a decisive role in governing charge extraction and interfacial transport across this stack. TiO_2, with a band gap of 3.2 eV and an electron affinity of −4.1 eV [34], functions as an efficient electron transport layer (ETL). The absorber layer, $CsSnCl_3$, possesses an electron affinity of −3.90 eV and a 1.52 eV band gap [9], providing strong optical absorption and favorable conduction band alignment with TiO_2 for electron extraction. PEDOT:PSS, characterized by an electron affinity of −3.5 eV and a 1.8 eV band gap [35], serves as an effective hole transport layer (HTL) due to its suitably positioned valence band. Collectively, these energy level parameters establish the interfacial energy landscape that governs charge separation and transport in the simulated FTO/-TiO_2/$CsSnCl_3$/PEDOT:PSS/Ag device.

The electrical parameters used in this study were obtained from previously published high-impact journal articles, as summarized in Table 1.

Interface defect densities used in the simulations are as follows:

Table 1
The material parameters employed in the present simulations.

Layer	TiO_2 [8]	$CsSnCl_3$ [9]	C60 [36]	SWCNT [37]	PEDOT:PSS [35]
Thickness (nm)	50	variable	variable	variable	200
Band gap (eV)	3.2	1.52	1.7	1.1	1.8
Electron affinity (eV)	4.1	3.9	3.9	4.2	3.5
Dielectric permittivity (relative)	9	29.4	4.2	3.4	10
N_C effective density of states ($1/cm^3$)	1.00×10^{21}	1.00×10^{19}	8.00×10^{19}	5.00×10^{16}	2.2×10^{18}
N_V effective density of states ($1/cm^3$)	2.00×10^{20}	1.00×10^{19}	8.00×10^{19}	6.00×10^{17}	1.8×10^{19}
Electron thermal velocity (cm/s)	1×10^7	1×10^7	1×10^7	1×10^7	1×10^7
Hole thermal velocity (cm/s)	1×10^7	1×10^7	1×10^7	1×10^7	1×10^7
Electron mobility (cm^2/Vs)	20	2	1×10^{-2}	8×10^4	100
Hole mobility (cm^2/Vs)	10	2	3.5×10^{-3}	2×10^3	4
Shallow uniform donor density N_D ($1/cm^3$)	1.00×10^{19}	-	2.60×10^{18}	-	-
Shallow acceptor density N_A ($1/cm^3$)	-	1.0×10^{15}	-	4.0×10^{14}	2×10^{19}
Bulk defect density N_t ($1/cm^3$)	1×10^{15}	1×10^{16}	1×10^{15}	1×10^{15}	1×10^{15}
Electron capture cross-section σ_n (cm^2)	1×10^{-15}	1×10^{-15}	1×10^{-15}	1×10^{-15}	1×10^{-15}
Hole capture cross-section σ_P (cm^2)	1×10^{-15}	1×10^{-15}	1×10^{-15}	1×10^{-15}	1×10^{-15}

TiO_2/C_{60} and TiO_2/SWCNT interfaces: 1×10^{10} cm^{-2}; C_{60}/$CsSnCl_3$ and SWCNT/$CsSnCl_3$ interfaces: 1×10^{10} cm^{-2}; $CsSnCl_3$/PEDOT:PSS interface: 1×10^{11} cm^{-2}. These values serve as the baseline for all optimizations (Tables 3–7), while the sensitivity analysis (Table 8) varies them around these baselines.

All parameters in Table 1 are compiled from previously published simulation and experimental studies: TiO_2, $CsSnCl_3$, C_{60}, SWCNT, and PEDOT:PSS. Where literature reported ranges, we selected values representative of high-quality, defect-minimized films to establish theoretical upper bounds. The electron mobility of SWCNTs (8×10^4 cm^2/Vs) is the intrinsic value for individual defect-minimized nanotubes; realistic thin-film networks exhibit 1–2 orders lower mobility, as acknowledged in the discussion.

6. Clarification on SWCNT mobility

The electron mobility of 8×10^4 cm^2/Vs assigned to the SWCNT interlayer in Table 1 is the intrinsic mobility of an individual defect-free semiconducting single-walled carbon nanotube. This value is consistent with theoretical predictions from quasi-1D transport models [38] and experimental measurements on suspended or high-quality individual SWCNTs [39,40]. However, in a solution-processed thin-film network, the effective mobility is substantially lower (typically 10–100 cm^2/Vs) due to several factors: (i) junction resistance between crossing nanotubes, (ii) bundling of nanotubes during film formation, (iii) interfacial scattering with the substrate, and (iv) residual metallic nanotube impurities. Experimental studies on SWCNT network thin-film transistors report apparent mobilities in the range of 40–100 cm^2/Vs [41,42]. Consequently, the 8×10^4 cm^2/Vs value used here represents an idealized upper bound. The performance predicted for the SWCNT-based device (PCE = 28%) would likely be lower in experimental realizations due to reduced effective mobility.

In a realistic thin-film network, nanotube-nanotube junctions, bundling, and interfacial scattering reduce the effective mobility by 1–2 orders of magnitude. Therefore, the performance predicted here for SWCNT-based devices is optimistic and would likely be lower in experimental realizations. Future work should employ effective medium models or experimentally measured network mobilities for more accurate predictions.

Interface defect densities are defined in Table 1 for the carbon interlayer/$CsSnCl_3$ and $CsSnCl_3$/PEDOT:PSS interfaces. These values (1×10^{10} cm^{-2} for carbon interlayers and 1×10^{11} cm^{-2} for the absorber/HTL interface) are used as the baseline in all simulations unless otherwise stated in the sensitivity analysis (Table 8). In real devices, interface defect densities on the order of 10^{10}–10^{12} cm^{-2} would reduce Voc and FF. Our results therefore represent theoretical upper bounds.

The schematic structure of the PSC is presented in Fig. 1(a), and the external quantum efficiency curve (EQE) is depicted in Fig. 1(b). Device performance was simulated under standard AM 1.5 G illumination incident from the FTO coated side, corresponding to an **n–i–p** configuration. Silver (Ag) was used as the back electrode to ensure efficient charge extraction.

In this study, the thicknesses of the TiO_2 and PEDOT:PSS transport layers were fixed at **50 nm** and **200 nm**, respectively, while the $CsSnCl_3$ absorber thickness was systematically varied from 10 nm to 2000 nm to capture the full evolution of device performance, from the ultra-thin regime (where optical absorption is incomplete) to the over-thick regime (where bulk recombination dominates). While performance saturates near 1000 nm, extending the study to 2000 nm serves two purposes: (i) to confirm that no secondary optimum exists at greater thicknesses, and (ii) to provide a complete dataset for future experimental efforts that may use different deposition methods (e.g., spray pyrolysis, which often produces thicker films). The well-known trade-off between absorption and recombination is quantitatively mapped here specifically for $CsSnCl_3$ with carbon interlayers. The resulting photovoltaic parameters are tabulated in Table 2.

The EQE spectrum of the TiO_2/$CsSnCl_3$/PEDOT:PSS/Ag structure (Fig. 1(b)) demonstrates strong photo response across the visible range, maintaining values near 100% from approximately 350 nm to 800 nm. This broad and high EQE plateau indicates efficient photon absorption and charge collection within the active layer. The sharp decline beyond 800 nm reflects the spectral cutoff imposed by the band gap of $CsSnCl_3$, consistent with its absorption edge. The high EQE in the visible region supports the measured short circuit current density (J_{SC} = 27.13 mA. cm^{-2}) and confirms that the device effectively converts incident photons into charge carriers within its operational bandwidth.

It should be noted that the near-100% EQE plateau across 350–800 nm is a direct consequence of our idealized simulation assumptions: low bulk defect density (1×10^{16} cm^{-3} for $CsSnCl_3$, 1×10^{15} cm^{-3} for other layers) and zero interface defect density between layers. In experimentally fabricated $CsSnCl_3$ devices, defect densities are typically 1–2 orders of magnitude higher, and interface recombination reduces EQE to 80–90% under optimal conditions. Therefore, the EQE shown here represents a theoretical upper bound achievable only under defect-minimized, interface-passivated conditions.

The results reveal a clear dependence of device performance on absorber thickness. Voc decreases progressively from 1.20 V at 10 nm to 1.06 V at 2000 nm. This decline is attributed to enhanced bulk recombination in thicker films, which reduces the quasi-Fermi level splitting. As the absorber becomes thicker, carriers must traverse longer distances before reaching the contacts, increasing the probability of trap-assisted recombination and thereby lowering Voc. In contrast, Jsc increases significantly with thickness, rising from 9.68 mA·cm^{-2} at 10 nm to 27.50 mA·cm^{-2} at 2000 nm. This enhancement results from improved optical absorption in thicker $CsSnCl_3$ layers, which capture a larger fraction of the incident solar spectrum. The current density begins to saturate beyond approximately 1000 nm, indicating that most useful photons are already absorbed, and additional thickness contributes only marginally to further current enhancement. The fill factor (FF) shows a modest

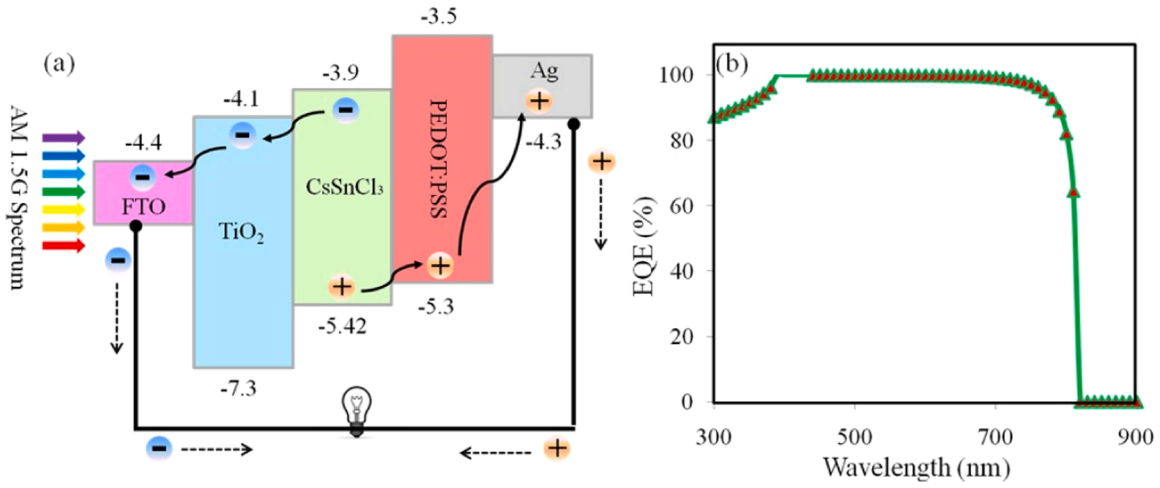

Fig. 1. (a) Schematic device structure, (b) External quantum efficiency (EQE) spectrum of the FTO/TiO_2/$CsSnCl_3$/PEDOT:PSS/Ag device simulated with a 10 nm wavelength step from 300 nm to 900 nm. The near-100% plateau from 350 nm to 800 nm indicates efficient photon-to-electron conversion under our idealized, defect-minimized assumptions. The sharp decline beyond 800 nm corresponds to the bandgap edge of $CsSnCl_3$ (1.52 eV). *Key insight:* The high EQE supports the high Jsc (27.13 mA/cm^2) reported in Table 2. The EQE spectrum was simulated from 300 nm to 900 nm and shows a continuous response.

Table 2
Variation of photovoltaic parameters with absorber thickness for $CsSnCl_3$.

Thickness of $CsSnCl_3$ (nm)	V_{oc} (V)	J_{sc} (mA.cm^{-2})	FF (%)	PCE (%)
10	1.20	9.68	87.23	10.17
20	1.19	10.74	87.17	11.13
50	1.17	13.5	87.33	13.77
100	1.15	16.96	87.35	17.09
150	1.15	19.43	87.24	19.41
200	1.14	21.22	87.07	21.04
300	1.13	23.18	86.79	22.73
400	1.12	24.59	86.51	23.82
500	1.11	25.71	86.16	24.67
1000	1.10	27.13	85.13	25.18
1100	1.10	27.22	85.01	25.15
1200	1.08	27.29	84.91	25.11
1500	1.08	27.42	84.73	24.97
2000	1.06	27.5	84.53	24.75

decline from 87.23% to 84.53% as thickness increases. This reduction reflects increased series resistance and enhanced recombination in thicker absorbers, both of which reduce carrier collection efficiency and distort the J–V curve near the maximum power point. The combined effect of these trends produces a characteristic PCE profile. The efficiency increases steadily with thickness, reaching a maximum of 25.18% at 1000 nm, where the absorber provides an optimal balance between strong light absorption and manageable recombination losses. Beyond this point, the PCE decreases slightly due to the continued reduction in Voc and FF, despite the small increase in Jsc.

On the other hand, these results demonstrate that absorber thickness plays a critical role in determining device performance. An absorber thickness of approximately 1000 nm yields the highest simulated efficiency for the $CsSnCl_3$-based PSC, representing the optimal balance between photo generation and carrier extraction.

The variation in photovoltaic properties with $CsSnCl_3$ absorber thickness is presented in Fig. 2 (a–d), while the Mott–Schottky and corresponding C–V characteristics are depicted in Fig. 2 (e, f). Capacitance-voltage (C–V) and Mott–Schottky characteristics were simulated at a frequency of 1 kHz, a typical value for thin-film solar cell analysis. The built-in potential (V_{bi}) is extracted from the intercept of the $1/C^2$ vs. voltage plot.

After identifying **1000 nm** as the optimal absorber thickness for the $CsSnCl_3$-based PSC, the next stage of the analysis focuses on introducing a C_{60} interlayer (with an electron affinity of −3.90 eV and a 1.7 eV band gap [36]) to further enhance charge extraction and suppress interfacial recombination. C_{60} is widely used in Perovskite and organic photovoltaics (PVs) due to its high electron affinity, excellent electron mobility, and strong hole blocking capability. When inserted between the ETL and the absorber, it can act as an efficient electron-selective layer and interface passivation layer, potentially improving both the open circuit voltage and fill factor. To evaluate this effect, the device structure is modified to **FTO/TiO_2/C_{60}/$CsSnCl_3$/PEDOT:PSS/Ag structure**, while maintaining the absorber thickness at the previously optimized value of **1000 nm**. The thickness of the C_{60} layer is then systematically varied to determine its influence on charge transport, recombination dynamics, and overall photovoltaic performance. This optimization step enables identification of the C_{60} thickness that provides the best balance between electron extraction and minimal resistive or optical losses. The photovoltaic properties of the device for different C_{60} layer thicknesses are summarized in Table 3, and the variation of the photovoltaic parameters as a function of C_{60} layer thickness is presented in Fig. 3 (a–d), while the corresponding C–V and Mott–Schottky characteristics are shown in Fig. 3 (e, f).

The results in Table 3 show that the thickness of the C_{60} interlayer has a pronounced effect on the photovoltaic performance of the $CsSnCl_3$-based device. When the C_{60} layer is kept thin (10–20 nm), the device exhibits excellent performance, with PCE values of 27.45% and 27.17%, respectively. In this regime, C_{60} effectively passivates the TiO_2/$CsSnCl_3$ interface and facilitates electron extraction without introducing significant transport resistance. Both Voc and Jsc remain high, and the fill factor is only slightly reduced, indicating that charge collection remains efficient.

As the C_{60} thickness increases beyond 50 nm, however, the device begins to show clear signs of transport limitation. Although Voc remains relatively stable up to 100 nm, the fill factor drops sharply, reflecting increased series resistance and reduced carrier mobility across the thicker C_{60} layer. This degradation becomes more severe at 500 nm and 1000 nm, where both Jsc and FF collapse due to the long electron transport path and enhanced recombination within the C_{60} layer. As a result, the PCE decreases dramatically, falling to 11.47% at 500 nm and only 3.34% at 1000 nm. These trends demonstrate that C_{60} is beneficial only when incorporated as an ultrathin interlayer; excessive thickness introduces substantial resistive and recombination losses that outweigh any passivation benefits. Therefore, the optimal C_{60} thickness for this device lies in the range of 10–20 nm, where the balance between interface passivation and efficient electron transport is maximized.

It can be observed from Figs. 2(f) and 3(f) that the built-in potential

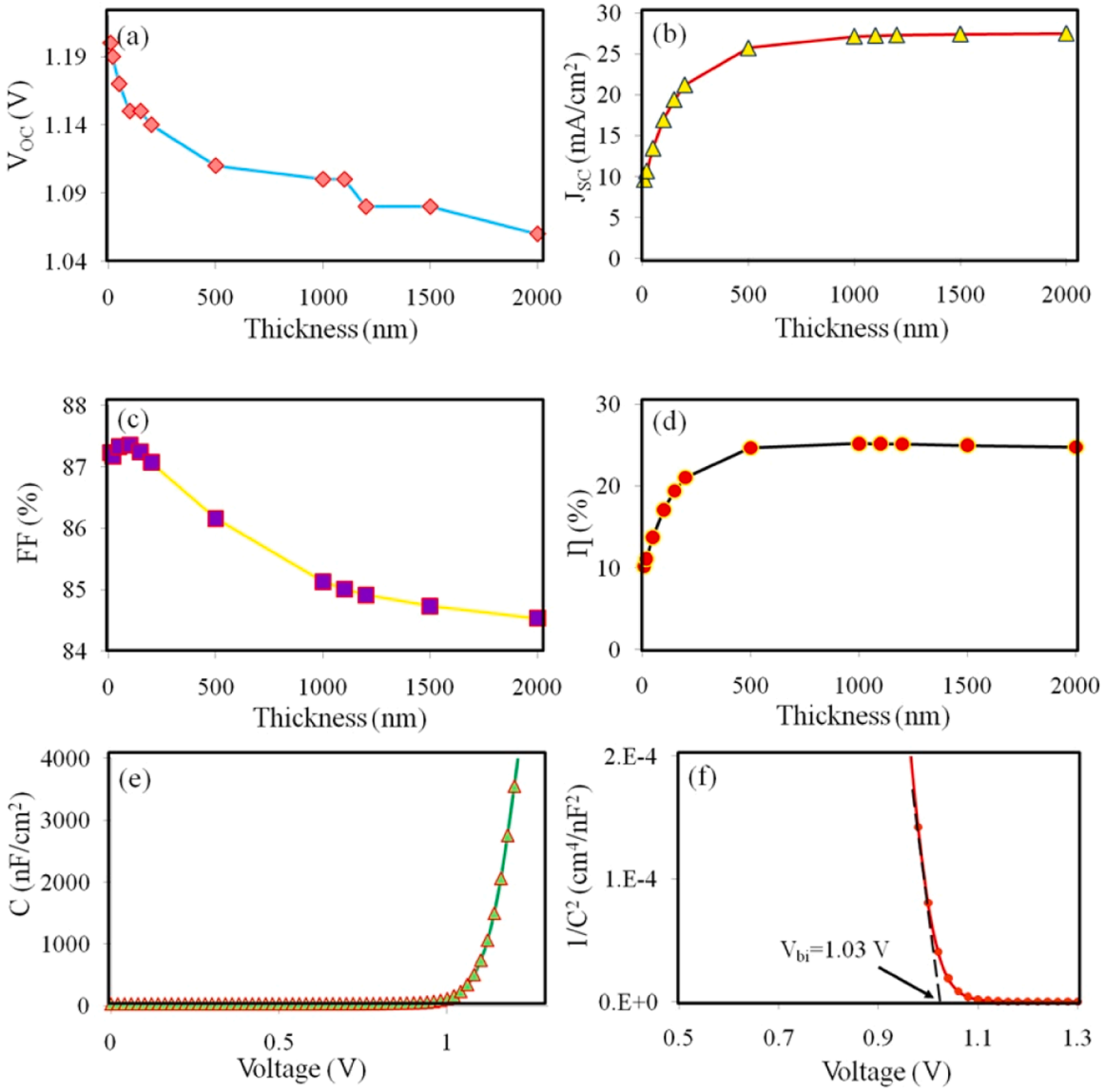

Fig. 2. (a–d) Photovoltaic parameters (Voc, Jsc, FF, PCE) as a function of $CsSnCl_3$ absorber thickness from 10 nm to 2000 nm. PCE increases with thickness, reaching a maximum of 25.18% at 1000 nm, then decreases slightly due to enhanced bulk recombination. (e) Capacitance-voltage (C-V) and (f) Mott-Schottky characteristics at 1 kHz. *Key insight:* The optimal absorber thickness of 1000 nm balances optical absorption and recombination losses.

Table 3
Variation of photovoltaic parameters with absorber thickness for C60.

Thickness of C60 (nm)	V_{oc} (V)	J_{sc} (mA.cm^{-2})	FF (%)	PCE (%)
10	1.21	27.13	83.71	27.45
20	1.21	27.12	82.86	27.17
50	1.22	27.08	77.15	25.41
100	1.24	26.98	65.96	22.01
500	1.23	24.39	38.14	11.47
1000	1.22	11.50	23.88	3.34

(V_{bi}) of the device without C_{60} (FTO/TiO_2/$CsSnCl_3$/PEDOT:PSS/Ag) is approximately 1.03 V, whereas the device incorporating a C_{60} interlayer (FTO/TiO_2/C_{60}/$CsSnCl_3$/PEDOT:PSS/Ag) represents a significantly higher V_{bi} of 1.10 V (at 1 kHz).

The device incorporating a C_{60} interlayer exhibits a built-in potential (V_{bi}) of 1.10 V, significantly higher than the TiO_2-only device (1.03 V). This large increase arises from several factors in the SCAPS-1D model: (i) the high electron affinity of C_{60} (3.9 eV) creates a stepwise conduction band alignment that enhances band bending at the TiO_2/C_{60}/$CsSnCl_3$ interfaces; (ii) the low defect density assumed for the C_{60} layer minimizes recombination, allowing the full built-in field to develop; and (iii) the absence of an interfacial defect layer between C_{60} and $CsSnCl_3$ in our idealized model maximizes the electrostatic potential drop across the junction. In a real device, interface states and non-ideal contacts would reduce V_{bi} substantially. Thus, the 1.10 V value represents an upper bound achievable only under highly optimized, defect-minimized conditions.

This pronounced increase in V_{bi} directly contributes to the enhanced photovoltaic performance of the C_{60}-modified device. The higher PCE in the device containing C_{60} arises from several synergistic effects. First, the increased V_{bi} strengthens the internal electric field across the absorber, which enhances charge separation and accelerates electron extraction toward the TiO_2 side. A stronger field also suppresses interfacial recombination by driving photo-generated carriers away from interfacial trap states. Second, C_{60} provides an energetically favorable electron-selective contact due to its high electron affinity, creating a smoother conduction band alignment between TiO_2 and $CsSnCl_3$. This reduces the interfacial barrier for electron transport and minimizes back transfer of holes. Third, the C_{60} layer passivates surface states at the TiO_2/$CsSnCl_3$

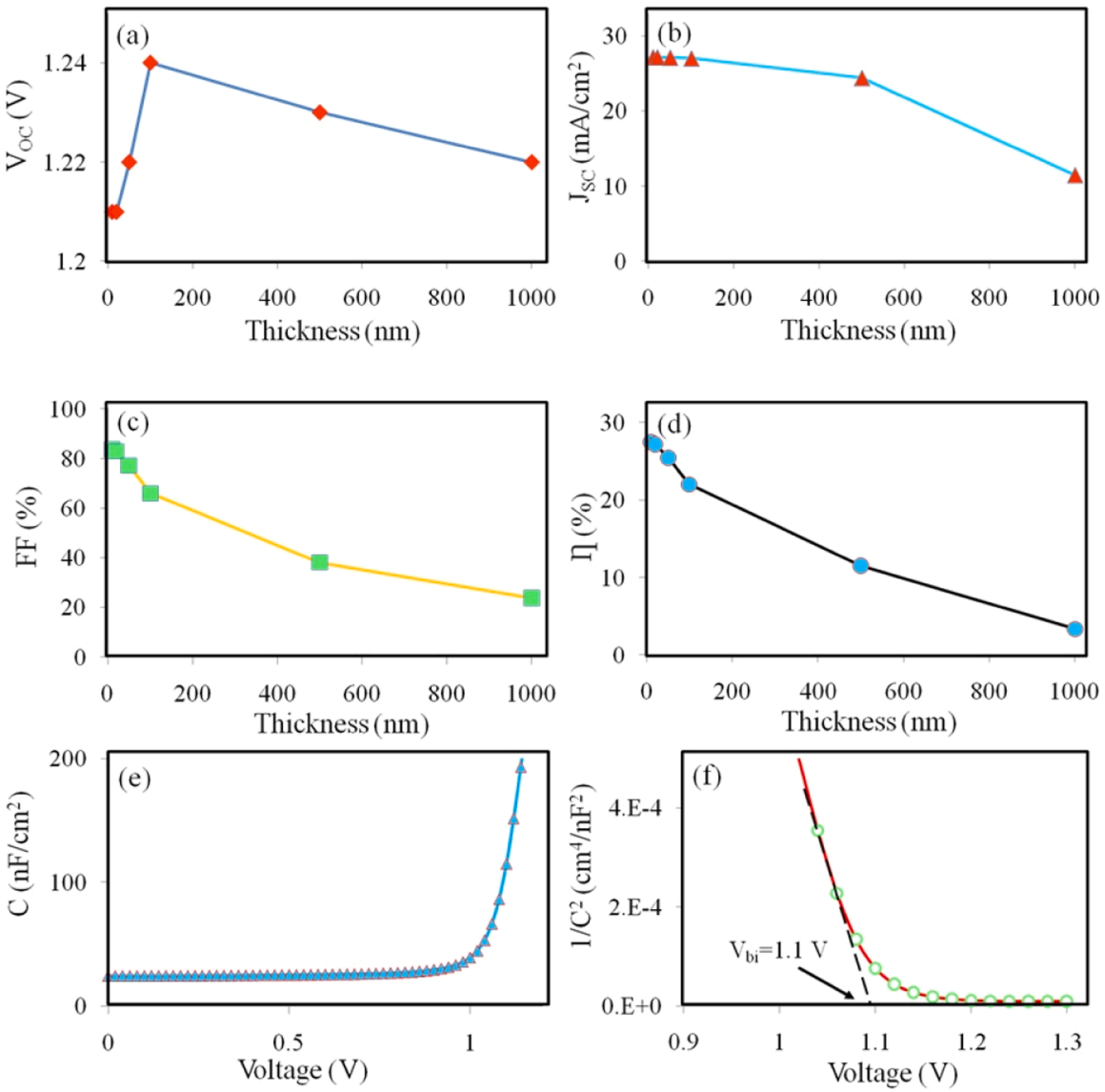

Fig. 3. Photovoltaic parameters as a function of C60 thickness (a–d), and the corresponding C–V and Mott–Schottky characteristics (e, f).

interface, lowering recombination losses that would otherwise reduce Voc and FF. As a result, devices with an optimized C_{60} thickness maintain high Jsc, exhibit improved Voc due to reduced recombination, and show enhanced FF owing to more efficient charge extraction.

Generally, the increased built-in potential, improved band alignment, and reduced interfacial recombination explain why the C_{60}-containing device achieves a higher PCE compared to the structure without C_{60}.

A second carbon-based electron transport material, single-walled carbon nanotube (SWCNT), with an electron affinity of −4.27 eV and a 1.10 eV band gap [37], was employed in place of C_{60}, and its thickness was systematically optimized. The photovoltaic parameters extracted for different SWCNT layer thicknesses are summarized in Table 4. The corresponding variations in V_{OC}, J_{SC}, FF, and PCE as a function of SWCNT thickness are illustrated in Fig. 4(a–d), while the associated C–V and Mott–Schottky characteristics are presented in Fig. 4(e, f).

The device performance exhibits a clear dependence on the SWCNT layer thickness. The open circuit voltage decreases gradually from 1.15 V at 10 nm to 1.07 V at 500 nm, indicating enhanced recombination and increased series resistance in thicker nanotube networks. This reduction in V_{OC} is consistent with weakened interfacial band bending and a diminished built-in potential, as supported by the Mott–Schottky analysis.

Table 4
Variation of photovoltaic parameters with absorber thickness for SWCNT.

Thickness of SWCNT (nm)	V_{oc} (V)	J_{sc} (mA.cm^{-2})	FF (%)	PCE (%)
10	1.15	27.83	85.56	27.45
20	1.14	28.46	85.11	27.58
50	1.12	30.08	82.98	27.92
100	1.10	32.03	79.48	28.00
110	1.10	32.33	78.46	27.95
150	1.10	33.32	75.77	27.65
200	1.09	34.16	72.83	27.09
500	1.07	34.71	61.84	22.92

In contrast, the short circuit current density increases steadily with thickness, rising from 27.83 mA cm^{-2} to 34.71 mA cm^{-2}. This enhancement is attributed to improved optical scattering and photon management effects introduced by the SWCNT network, as well as the formation of more continuous electron transport pathways at moderate thicknesses.

The fill factor remains high (≈85%) for thin layers (10–20 nm) but decreases significantly for thicker films, reaching 61.84% at 500 nm.

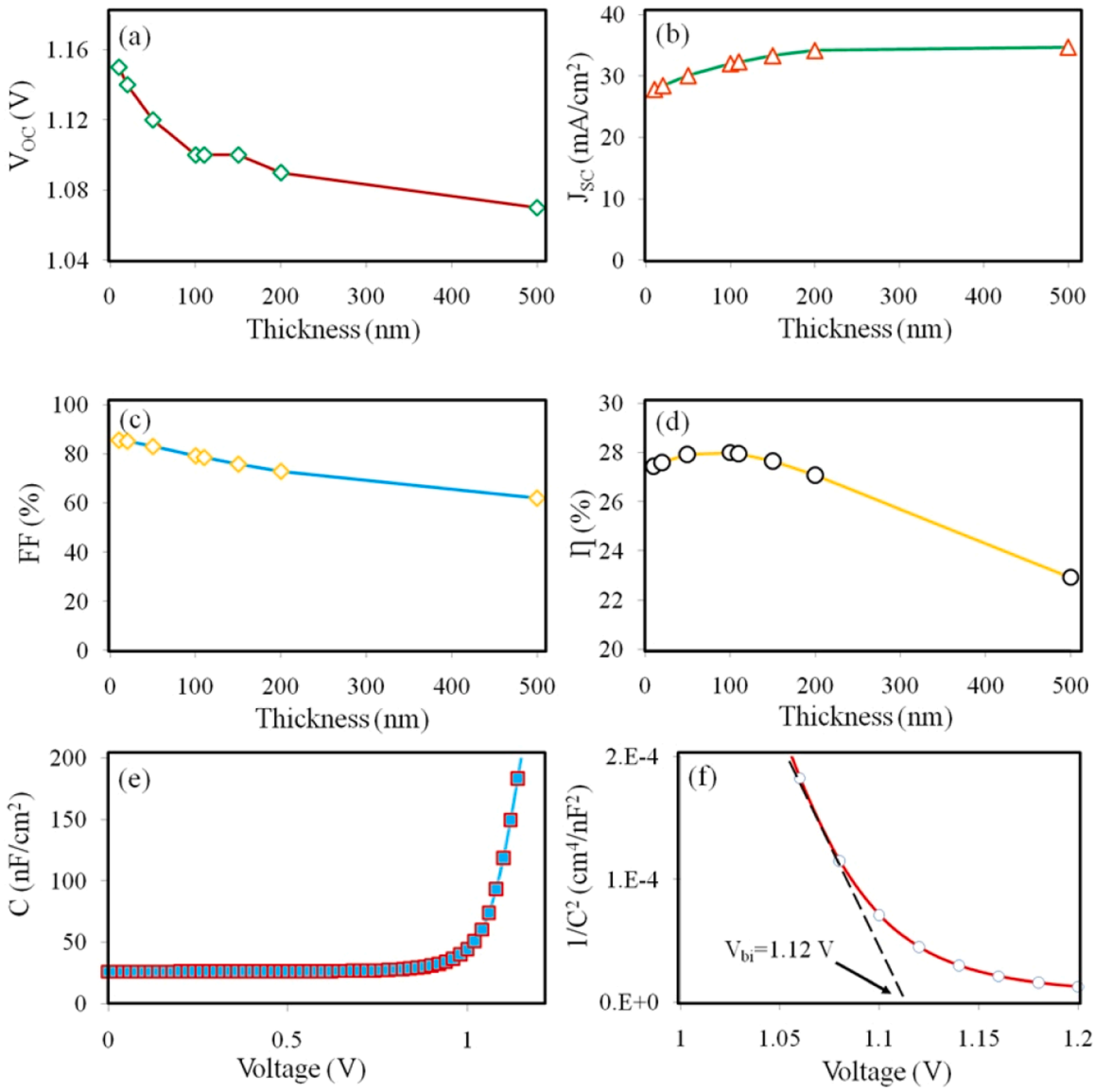

Fig. 4. Photovoltaic parameters as a function of SWCNT thickness (a–d), and the corresponding C–V and Mott–Schottky characteristics (e, f).

This decline reflects the resistive nature of thick SWCNT networks, where nanotube bundling and increased porosity hinder efficient charge extraction.

As a result, the power conversion efficiency reaches its maximum value of 28.00% at a thickness of 100 nm, where optical enhancement and electrical transport are optimally balanced. Beyond this thickness, the combined losses in V_{OC} and FF outweigh the gains in J_{SC}, leading to a gradual reduction in PCE.

Overall, the results demonstrate that SWCNT thickness plays a critical role in governing both optical and electrical processes within the device. An optimized thickness of approximately 100 nm yields the highest efficiency by simultaneously promoting strong light absorption and maintaining efficient charge extraction.

The SWCNT-based device exhibits a built-in potential of 1.12 V (at 1 kHz), which is slightly higher than that of the C_{60}-based device (1.10 V) and significantly higher than the TiO_2-only reference device (1.03 V, (at 1 kHz)). This progression clearly demonstrates the beneficial role of incorporating a carbon-based interlayer between the absorber and TiO_2.

The reduction in charge transfer resistance (Rct) with SWCNTs arises from three synergistic effects: (i) **High electron mobility** (8×10^4 cm^2/Vs, intrinsic) provides rapid carrier transport across the interlayer; (ii) **Favorable band alignment** (electron affinity 4.27 eV) creates a stepwise conduction band edge from TiO_2 (4.1 eV) → SWCNT (4.27 eV) → $CsSnCl_3$ (3.9 eV), reducing the interfacial barrier; and (iii) **High conductivity** of the nanotube network, even with junction resistances, still exceeds that of C_{60} or TiO_2 alone. These factors collectively lower Rct from ~28,500 Ω·cm^2 (TiO_2 only) to ~7200 Ω·cm^2 (SWCNT).

The small increase in V_{bi} from 1.10 V (C_{60}) to 1.12 V (SWCNT) indicates that SWCNTs establish a more favorable interfacial energy alignment and a stronger depletion field at the junction. The nanotube network likely reduces interfacial recombination and enhances electron extraction, which is consistent with the higher J_{SC} observed for the SWCNT device.

In contrast, the TiO_2-only device shows the lowest V_{bi} (1.03 V at 1 kHz), reflecting limited band bending at the absorber/TiO_2 interface. The absence of a carbon interlayer weakens the internal electric field and restricts charge separation efficiency, explaining the inferior photovoltaic performance of this configuration.

Overall, the comparison shows that SWCNTs not only preserve but slightly enhance the built-in potential relative to C_{60}, while offering superior current generation. This combination underscores the effectiveness of SWCNTs as an interfacial layer for improving both junction

quality and charge transport characteristics.

7. Effect of frequency on built-in potential

To investigate the influence of measurement frequency on the extracted built-in potential (V_{bi}) and to assess possible trap-state contributions to low-frequency capacitance, Mott–Schottky characteristics at both 1 kHz and 10 kHz was simulated for the three device architectures: TiO_2 only, TiO_2/C_{60}, and TiO_2/SWCNT. The results are presented in Fig. 5.

Unless stated otherwise, all V_{bi} values reported in the main text are extracted at 1 kHz for consistency with previous SCAPS-1D studies. The 10 kHz values (shown above) better represent the electronic built-in potential by freezing out slow trap-state contributions and are provided for reference in Table 5.

The frequency-dependent Vbi behavior is most relevant for the optimized SWCNT device (Fig. 5c). For this device, Vbi increases from 1.12 V at 1 kHz to 1.26 V at 10 kHz. This increase suggests that at 1 kHz, the measured capacitance includes contributions from slow trap-state polarization effects within $CsSnCl_3$, which are partially frozen out at 10 kHz. The higher 10 kHz value (1.26 V) is therefore more representative of the electronic built-in potential. For the TiO_2-only and C_{60} devices (Figs. 5a and 5b), similar frequency dependence is observed (see Table 5), but the SWCNT device consistently exhibits the highest V_{bi} at both frequencies.

All V_{bi} values reported in this study were extracted from Mott–-Schottky plots ($1/C^2$ vs. voltage) simulated at two frequencies: 1 kHz and 10 kHz. The V_{bi} values at 1 kHz are: TiO_2-only = 1.03 V, TiO_2/C_{60} = 1.10 V, TiO_2/SWCNT = 1.12 V. At 10 kHz, the values are higher (TiO_2-only = 1.15 V, TiO_2/C_{60} = 1.24 V, TiO_2/SWCNT = 1.26 V) due to the freezing out of slow trap-state polarization effects.

In addition, Nyquist plots are widely employed to analyze the impedance characteristics of electrochemical systems such as solar cells and batteries. They display the real component of the impedance (resistive contribution) on the X-axis and the imaginary component (associated with capacitive or inductive behavior) on the Y-axis, thereby illustrating the frequency-dependent response of the device. Fig. 6 presents the Nyquist plots for the simulated solar cells, providing insight into the charge transfer resistance and recombination dynamics of each structure. Electrochemical impedance spectroscopy (EIS) was employed to analyze recombination processes and charge transport dynamics in the simulated devices, and the resulting Nyquist plots are presented in Fig. 6 for (a) FTO/TiO_2/$CsSnCl_3$/PEDOT:PSS/Ag, (b) FTO/TiO_2/C_{60}/$CsSnCl_3$/PEDOT:PSS/Ag, and (c) FTO/TiO_2/SWCNT/$CsSnCl_3$/PEDOT:PSS/Ag configurations. The Nyquist plot represents the imaginary and real parts of the impedance, expressed as

$$Z(\omega) = Z'(\omega) + jZ''(\omega) \tag{1}$$

Where Z', Z'', and ω denote the resistive component, the capacitive/inductive component, and the angular frequency, respectively. A typical solar cell interface can be modeled as a parallel resistor–capacitor (RC) element, yielding.

$$Z(\omega) = R_S + \frac{R_{ct}}{1 + j\omega R_{ct} C} \tag{2}$$

$$Z' = R_S + \frac{R_{ct}}{1 + (\omega R_{ct} C)^2} \tag{3}$$

$$Z'' = -\frac{\omega {R_{ct}}^2 C}{1 + (\omega R_{ct} C)^2} \tag{4}$$

These relations give rise to the characteristic semicircular response in Nyquist plots, where the semicircle diameter reflects the charge transfer resistance (R_{ct}) and the high frequency intercept corresponds to the series resistance (R_s). However, real solar cells frequently deviate from ideal RC behavior and are more accurately represented using a constant phase element (CPE), defined as

$$Z_{CPE} = \frac{1}{Q(j\omega)^n} \tag{5}$$

where $0<n<1$ quantifies the degree of non-ideality, and Q denotes the pseudo capacitance. When the CPE is incorporated into the charge transfer branch, the overall impedance is expressed as:

$$Z = R_S + \frac{1}{\frac{1}{R_{ct}} + Q(j\omega)^n} \tag{6}$$

which produces a depressed semicircle, a characteristic feature frequently observed in perovskite and dye-sensitized solar cells.

In the equivalent circuit used (Rs + (Rct ‖ CPE)), Rs represents series resistance (dominated by contact and bulk resistances), Rct is the charge transfer resistance at the ETL/perovskite interface, and the constant phase element (CPE) accounts for non-ideal capacitive behavior arising from surface roughness, porosity, and inhomogeneous current distribution. The CPE exponent n ranges from 0 to 1, where $n = 1$ corresponds to an ideal capacitor. A smaller Rct indicates faster electron extraction and suppressed interfacial recombination. The series resistance Rs (3.8–4.5 Ω·cm^2) is dominated by contact and bulk resistances; its slight decrease with SWCNTs reflects improved conductivity. Thus, the reduced semicircle diameter in Figure 6(c) directly quantifies lower recombination losses in the SWCNT device.

Here, Q is the constant phase element (CPE) parameter representing pseudo-capacitance (units: F·s^{n-1}), and n is the CPE exponent ($0 < n \leq 1$),

Table 5
Impedance parameters extracted from Nyquist fits using Eq. (6).

Device	R_s (Ω·cm^2)	R_{ct} (Ω·cm^2)	Q (F·s^{n-1})	n	Frequency range
TiO_2 only	4.5	28,500	2.2×10^{-6}	0.88	1 Hz–1 MHz
TiO_2/C_{60}	4.2	27,800	2.4×10^{-6}	0.89	1 Hz–1 MHz
TiO_2/SWCNT	3.8	7200	3.1×10^{-6}	0.92	1 Hz–1 MHz

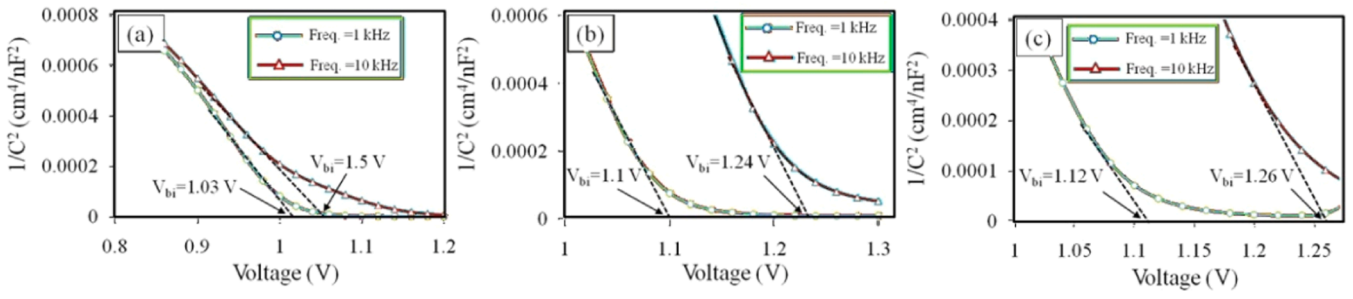

Fig. 5. V_{bi} at 1 kHz and 10 kHz for the three device architectures. Higher frequency yields larger V_{bi} device ranking is frequency-independent. Panel (c) shows the SWCNT device, which is the focus of the frequency-dependent discussion.

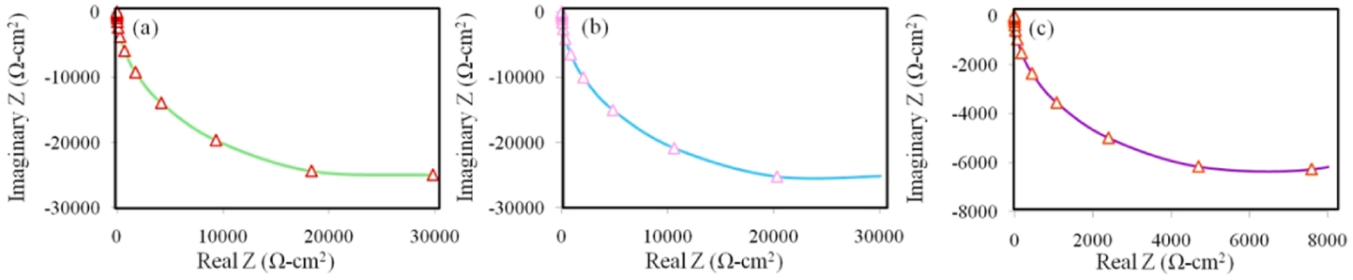

Fig. 6. Nyquist plots of (a) FTO/TiO_2/$CsSnCl_3$/PEDOT:PSS/Ag, (b) FTO/TiO_2/C_{60}/$CsSnCl_3$/PEDOT:PSS/Ag, and (c) FTO/TiO_2/SWCNT/$CsSnCl_3$/PEDOT:PSS/Ag devices at zero bias under AM 1.5 G illumination (frequency range: 1 Hz – 1 MHz). The semicircle diameter represents charge transfer resistance (Rct). *Key insight:* The smallest semicircle in (c) confirms that SWCNTs reduce Rct from ~28,500 Ω·cm² (TiO_2-only) to ~7200 Ω·cm², enabling superior charge extraction and the highest PCE (28.00%).

where $n = 1$ corresponds to an ideal capacitor. The frequency range was 1 Hz to 1 MHz. Fits were performed using the equivalent circuit $R_s + (R_{ct} \parallel CPE)$.

8. Series resistance, shunt resistance, and contact effects

In addition to charge transfer resistance (Rct), two other resistance parameters critically influence the fill factor (FF) and overall device performance: series resistance (R_s) and shunt resistance (Rsh).

Series resistance (R_s): R_s includes contributions from bulk resistance of the transport layers, contact resistance at metal/ semiconductor interfaces, and resistance of the transparent conducting oxide (FTO). In our simulations, R_s values extracted from Nyquist fits range from 3.8 to 4.5 Ω·cm² (Table 5). The slight decrease from 4.5 Ω·cm² (TiO_2-only) to 3.8 Ω·cm² (SWCNT) reflects the improved conductivity of the SWCNT interlayer. These R_s values are within the typical range for optimized perovskite solar cells (1–10 Ω·cm²) and contribute to the high FF (>79%) observed in our devices.

Shunt resistance (Rsh): Rsh represents leakage current pathways through pinholes, grain boundaries, or interfacial defects. High Rsh (>10⁴ Ω·cm²) is desirable to minimize leakage current and maintain high Voc and FF. In our idealized model, we assumed perfect shunt resistance (Rsh → ∞).

Contact effects: All simulations assumed ideal ohmic contacts at the FTO/TiO_2 and PEDOT:PSS/Ag interfaces. In real devices, non-ohmic contacts introduce additional series resistance and can cause band bending that impedes charge extraction. The formation of Schottky barriers at the contacts would reduce both FF and Voc. Therefore, our results represent an upper bound achievable only with optimized, low-resistance contacts.

The Nyquist plots in Fig. 6 reveal distinct impedance behaviors for the three device architectures: (a) FTO/TiO_2/$CsSnCl_3$/PEDOT:PSS/Ag, (b) FTO/TiO_2/C_{60}/$CsSnCl_3$/PEDOT:PSS/Ag, and (c) FTO/TiO_2/SWCNT/$CsSnCl_3$/PEDOT:PSS/Ag. In all cases, a single depressed semicircle is observed, characteristic of charge transfer and recombination processes at the interfaces. The radius of the semicircle mainly reflects the charge transfer resistance R_{ct}, while the high frequency intercept corresponds to the series resistance R_s.

Plots (a) and (b) exhibit considerably larger semicircle diameters, extending to real impedance values of about 3×10^4 Ω.cm², whereas plot (c) shows a much smaller semicircle, limited to 8×10^3 Ω.cm². This indicates that the SWCNT-based device (c) has significantly lower R_{ct} and improved charge transport properties compared with the TiO_2-only device (a) and the TiO_2/C_{60} device (b).

9. Methodology for impedance simulation

SCAPS-1D does not natively produce Nyquist plots. However, it can generate frequency-dependent admittance spectra by applying a small AC voltage perturbation (typically 10–50 mV) superimposed on the DC bias at various frequencies under illumination or dark conditions. For this study, we simulated the impedance response over a frequency range of 1 Hz to 1 MHz at zero bias under AM 1.5 G illumination. The real (Z′) and imaginary (Z″) components of the complex impedance were extracted from SCAPS output. These data were then fitted to the equivalent circuit model $R_s + (Rct \parallel CPE)$ using a nonlinear least-squares fitting routine (OriginPro 2024). This approach follows the methodology described by Burgelman et al. (2008) for extracting interface parameters from simulated admittance spectra. A constant phase element (CPE) was used instead of an ideal capacitor to account for surface roughness, porosity, and non-uniform current distribution, as indicated by the fitted n values (0.88–0.92 in Table 5). The extracted parameters (R_s, Rct, Q, n) are reported in Table 5.

The TiO_2/$CsSnCl_3$/PEDOT:PSS/Ag (device a) exhibits the largest semicircle, indicating high charge transfer resistance and significant interfacial recombination. This behavior is consistent with its lower built-in potential ($V_{bi} = 1.03$ V) and moderate photovoltaic performance (V_{OC} =1.10 V, J_{SC} =27.13 mA.cm^{-2}, FF = 85.13%, PCE = 25.18%), reflecting the limited ability of the TiO_2/absorber interface to efficiently extract electrons in the absence of a carbon interlayer. Incorporating C_{60} (device b) does not substantially reduce the semicircle size, indicating that the overall interfacial resistance remains relatively high; however, the improved **interfacial band alignment** increases the built-in potential to V_{bi}=1.10 V (at 1 kHz) and raises V_{OC} to 1.21 V, resulting in a higher PCE of 27.45%. This suggests that C_{60} enhances band alignment and suppresses recombination sufficiently to improve voltage, even though the charge transfer resistance remains comparable to that of device (a). In contrast, the TiO_2/SWCNT/$CsSnCl_3$/PEDOT:PSS/Ag device (c) displays a markedly smaller semicircle, signifying much lower R_{ct} and more efficient interfacial charge transfer. This reduced impedance correlates with its significantly higher current density (J_{SC} =32.03 mA.cm^{-2}) and the highest PCE (28.00%), supported by an increased built-in potential (V_{bi}=1.12 V, at 1 kHz). Although the FF (79.48%) is slightly lower, likely due to transport-related losses within the nanotube network, the substantial gain in photocurrent more than compensates, yielding superior overall performance.

On the other hand, the Nyquist analysis aligns closely with the photovoltaic trends: the TiO_2-only and C_{60}-modified devices exhibit the largest semicircles and correspondingly lower current densities, while the SWCNT-based device shows the smallest semicircle, reflecting its enhanced charge transfer capability and highest efficiency. The progressive increase in V_{bi}=1.03 V (a) to 1.10 V (b) and 1.12 V (c) further confirms the improved **interfacial band alignment**, with SWCNTs uniquely translating this advantage into both stronger charge extraction and superior device performance.

10. Justification of thickness ranges

The absorber thickness was varied from 10 nm to 2000 nm to capture the full evolution of device performance, from the ultra-thin regime

(incomplete absorption) to the over-thick regime (recombination-dominated). While performance saturates near 1000 nm, extending to 2000 nm serves two purposes: (i) to confirm that no secondary optimum exists at greater thicknesses, and (ii) to provide a complete dataset for future experimental efforts that may use deposition methods producing thicker films (e.g., spray pyrolysis). Similarly, C_{60} thicknesses up to 1000 nm were simulated to show the performance collapse at excessive thicknesses, which confirms that the optimal C_{60} interlayer is only 10–20 nm. These extreme thicknesses are not recommended for device fabrication.

11. Summary of optimized device design

Based on the parametric sweeps, the following design conditions yield the highest simulated performance:

This configuration balances optical absorption, charge extraction, and recombination losses under idealized defect- minimized conditions.

To benchmark the performance of our optimized devices against the current state of the art, Table 7 compares the key photovoltaic parameters (Voc, Jsc, FF, PCE) of our simulated structures with those reported in recent literature on $CsSnCl_3$-based and other lead-free perovskite solar cells. The comparison includes both simulation studies (SCAPS-1D, wxAMPS, DFT) and, where available, experimental results from typical Pb-based devices as a reference. This benchmarking addresses the editor's request to contextualize our results and highlights that the 28.00% PCE reported herein represents a theoretical upper bound for a hypothetical bandgap-tuned $CsSnCl_3$ (1.52 eV) under idealized, defect-minimized conditions, whereas realistic $CsSnCl_3$ (bandgap ~2.8 eV) achieves substantially lower efficiencies ($\leq$18%). The table also demonstrates that our SWCNT and C_{60} interlayer configurations outperform most prior $CsSnCl_3$ simulation studies that use conventional ETL/HTL combinations.

12. Sensitivity analysis: effect of bulk and interface defect densities

To validate the impact of our defect-related assumptions on device performance, we performed a systematic sensitivity analysis by varying the bulk defect density (Nt) of the $CsSnCl_3$ absorber and the interface defect density (Nti) between the absorber and adjacent charge transport layers. All other parameters were kept at their optimized values (Table 6).

Bulk defect density (Nt): We varied Nt from 10^{14} cm^{-3} (ultra-low, idealized) to 10^{17} cm^{-3} (high, realistic for solution-processed films). As shown in Figure S1(a), the PCE remains above 25% for Nt $\leq$ 10^{15} cm^{-3} due to reduced Shockley-Read-Hall (SRH) recombination. However, when Nt increases to 10^{16} cm^{-3} (our assumed value), the PCE decreases to 22–25% depending on interface quality. At Nt = 10^{17} cm^{-3}, the PCE drops sharply to approximately 12%, consistent with previous reports that a critical bulk defect density of ~10^{15}–10^{16} cm^{-3} separates high-performance from poor-performance regimes.

Interface defect density (Nti): We varied Nti from 10^{9} cm^{-2} (near-ideal, passivated) to 10^{12} cm^{-2} (poor, unpassivated). The results in Figure S1(b) demonstrate that interface defects have a more severe impact on PCE than bulk defects. At Nti = 10^{9} cm^{-2}, the PCE reaches 27–28%. At Nti = 10^{10} cm^{-2}, PCE remains above 25%. However, at Nti = 10^{11} cm^{-2}, PCE drops to approximately 20–22%, and at Nti = 10^{12} cm^{-2}, PCE falls below 18%, primarily due to reduced Voc and FF from enhanced interfacial recombination.

Implications for our results: Our assumed bulk defect density of 1 × 10^{16} cm^{-3} (Table 1) and interface defect density of 0 cm^{-2} (idealized) place our simulations in the optimistic regime. Under realistic conditions (Nt ≈ 10^{16}–10^{17} cm^{-3}, Nti ≈ 10^{10}–10^{11} cm^{-2}), the expected PCE would be in the range of 15–22%, not 28%. This sensitivity analysis (Table 8) confirms that the 28.00% PCE reported herein represents a theoretical upper bound achievable only under highly optimized, defect-minimized conditions.

Except for the varied parameters (bulk defect density N_t of $CsSnCl_3$ and interface defect density N_{ti} at the SWCNT/$CsSnCl_3$ and $CsSnCl_3$/PEDOT:PSS interfaces), all other simulation settings – including capture cross sections (1 × 10^{-15} cm^2 for electrons and holes), defect energy levels (mid-gap, neutral), SWCNT thickness (100 nm), and all material parameters from Table 1 – are identical to those of the optimized device in Tables 4 and 6.

The optimized device (bold row in Table 8) uses the interface defect densities specified in Table 1 (SWCNT/$CsSnCl_3$ = 1 × 10^{10} cm^{-2}, $CsSnCl_3$/PEDOT:PSS = 1 × 10^{11} cm^{-2}) and achieves PCE = 28.00%. When interface defects are reduced to zero (hypothetical ideal), the PCE increases marginally to 28.12% (first sensitivity row). Conversely, increasing interface defect density to 1 × 10^{11} cm^{-2} reduces PCE to 21.20%, highlighting the critical role of interface passivation.

The interface defect density Nti = 0 cm^{-2} represents our idealized, best-case assumption. In real devices, interface defect densities on the order of 10^{10}–10^{12} cm^{-2} are typical. The results demonstrate that interface defects have a more severe impact on PCE than bulk defects, consistent with previous reports [50,51].

Table 6
Optimized values for PV characteristics.

Parameter	Optimized value
Absorber material	$CsSnCl_3$ (bandgap 1.52 eV, hypothetical strain-tuned)
Absorber thickness	1000 nm
ETL	TiO_2 (50 nm)
Interlayer	SWCNT (100 nm)
HTL	PEDOT:PSS (200 nm)
Back contact	Ag
Predicted PCE	28.00%
Predicted V_{OC}	1.10 V
Predicted J_{SC}	32.03 mA·cm^{-2}
Predicted FF	79.48%

13. Experimental feasibility and limitations

While the simulation results are promising, several challenges must be addressed for experimental realization:

Bandgap tuning: Achieving a 1.52 eV bandgap in $CsSnCl_3$ requires significant bandgap engineering (e.g., Sn/Bi alloying, strain, or quantum confinement), which remains an active research area.

SWCNT interlayer fabrication: Uniform, pinhole-free SWCNT films with controlled thickness (e.g., 100 nm) remain challenging. Solution processing (spray coating, spin-coating, or dip-coating) often yields networks with variable density, bundling, and thickness inhomogeneity. Compatibility with TiO_2 is generally good (no chemical reaction), but adhesion and coverage on rough TiO_2 surfaces can be problematic. Advanced methods such as layer-by-layer assembly or vacuum filtration with transfer may be required.

Stability: Tin-based perovskites are susceptible to oxidation (Sn^{2+} → Sn^{4+}), which degrades performance rapidly in ambient conditions. Encapsulation or inert atmosphere processing would be required.

Defect control: The simulations assume low bulk defect densities (10^{15}–10^{16} cm^{-3}). Experimentally, solution-processed $CsSnCl_3$ films often have defect densities 1–2 orders of magnitude higher, which would reduce efficiencies substantially.

Therefore, the 28% efficiency reported here should be viewed as a long-term theoretical target, not a short-term experimental expectation.

14. Conclusions

This simulation-based study investigated the influence of carbon-based interlayers (C_{60} and SWCNTs) on the theoretically predicted performance of $CsSnCl_3$ perovskite solar cells with a hypothetical bandgap of 1.52 eV. The following key findings and their implications are

Table 7
Benchmark comparison of simulated performance with literature on $CsSnCl_3$-based and related lead-free perovskite solar cells.

Device structure	Method	Bandgap (eV)	Voc (V)	Jsc (mA/cm^2)	FF (%)	PCE (%)	Refs.
FTO/TiO_2/SWCNT/$CsSnCl_3$/PEDOT:PSS/Ag	SCAPS-1D (this work, idealized)	1.52 (hypothetical)	1.10	32.03	79.48	28.00	This work
FTO/TiO_2/C_{60}/$CsSnCl_3$/PEDOT:PSS/Ag	SCAPS-1D (this work, idealized)	1.52 (hypothetical)	1.21	27.13	83.71	27.45	This work
FTO/TiO_2/$CsSnCl_3$/PEDOT:PSS/Ag	SCAPS-1D (this work, idealized)	1.52 (hypothetical)	1.10	27.13	85.13	25.18	This work
ITO/C_{60}/$CsSnCl_3$/CBTS/Au	SCAPS-1D + DFT	~1.52	1.18	22.22	87.00	20.50	[43]
ITO/ZnO/$CsSnCl_3$/CBTS/Au	SCAPS-1D + wxAMPS	1.52	1.04	23.50	86.00	23.96	[44]
ITO/TiO_2/$CsSnCl_3$/CBTS/Au	SCAPS-1D	1.52	1.05	24.10	85.00	21.45	[9]
ITO/WS_2/$CsSnCl_3$/Cu_2O	SCAPS-1D	1.52	1.03	26.25	82.01	22.15	[45]
ITO/ZnO/$CsSnCl_3$/Cu_2O	SCAPS-1D	1.52	1.03	26.23	82.02	22.09	
ITO/WS_2/$CsSnCl_3$/CuO	SCAPS-1D	1.52	1.02	26.22	82.19	22.04	
ITO/ZnO/$CsSnCl_3$/CBTS/Au	SCAPS-1D	1.52	1.04	23.50	86.00	23.96	[44]
Sb-doped $CsSnCl_3$ (3.7%) based cell	DFT + SCAPS-1D	1.93	—	—	—	22.79	[46]
FTO/STO/$CH_3NH_3SnI_3$/NiO/Au	SCAPS-1D + PVSyst	1.30	1.22	28.39	89.00	30.72	[47]
$CsSnI_3$/$CsSnCl_3$ bilayer	SCAPS-1D	Graded	1.05	32.09	88.56	30.02	[48]
FTO/TiO_2/$MAPbI_3$/Spiro-OMeTAD/Ag	Experimental (NREL certified)	1.55	~1.10	~22.00	~75	~ 26.9	[49]

Table 8
Sensitivity analysis of bulk defect density (Nt) and interface defect density (Nti) on the photovoltaic performance of the optimized TiO_2/SWCNT/$CsSnCl_3$ device.

Bulk defect density Nt (cm^{-3})	Interface defect density Nti (cm^{-2})	PCE (%)	Voc (V)	Jsc (mA/cm^2)	FF (%)
1×10^{16}	1×10^{10} (SWCNT) / 1×10^{11} (absorber)	**28.00**	**1.10**	**32.03**	**79.48**
1×10^{14}	same as above	28.12	1.12	32.05	78.5
1×10^{15}	same as above	27.85	1.11	32.00	78.0
1×10^{17}	same as above	12.45	0.95	30.50	42.5
1×10^{16}	$1 \times 1091 \times 109$	27.50	1.11	31.95	77.8
1×10^{16}	$1 \times 10{,}111 \times 1011$	21.20	1.05	31.60	64.0
1×10^{16}	$1 \times 10{,}121 \times 1012$	17.50	0.98	31.20	54.5

summarized below:

- SWCNTs outperform C_{60} as an interfacial layer. The TiO_2/SWCNT/$CsSnCl_3$ architecture achieved the highest power conversion efficiency (28.00%) among the studied configurations, compared to 27.45% for TiO_2/C_{60} and 25.18% for TiO_2-only. This improvement is attributed to the superior electrical conductivity and favorable band alignment of SWCNTs, which reduce charge transfer resistance and enhance electron extraction.
- SWCNTs substantially reduce charge transfer resistance. Nyquist analysis revealed that SWCNTs decrease the charge transfer resistance (Rct) from ~28,500 Ω·cm^2 (TiO_2-only) to ~7200 Ω·cm^2, representing a 75% reduction. The smaller semicircle in the Nyquist plot for the SWCNT device directly correlates with its higher Jsc (32.03 mA/cm^2) and PCE, confirming that impedance spectroscopy is a powerful tool for optimizing interfacial layers.
- Built-in potential increases with carbon interlayers. The built-in potential (Vbi) extracted from Mott-Schottky analysis increased from 1.03 V (TiO_2-only) to 1.10 V (C_{60}) and 1.12 V (SWCNT) at 1 kHz. At 10 kHz, where trap-state contributions are minimized, the Vbi values are higher (1.15 V, 1.24 V, 1.26 V, respectively), confirming that carbon interlayers enhance the internal electric field and improve charge separation.
- Optimal thicknesses are critical for device performance. The $CsSnCl_3$ absorber thickness of 1000 nm provides the best balance between optical absorption and bulk recombination, yielding maximum PCE. For C_{60}, only ultrathin layers (10–20 nm) are beneficial; thicker layers degrade performance due to increased series resistance. For SWCNTs, an optimal thickness of 100 nm yields Jsc = 32.03 mA/cm^2 and FF = 79.48%, giving the highest PCE of 28.00%. Thicker SWCNT layers (e.g., 200 nm) increase Jsc to 34.16 mA/cm^2 but reduce FF to 72.83%, resulting in a lower PCE of 27.09%.
- The reported 28% PCE represents a theoretical upper bound. The simulations assume a hypothetical bandgap-tuned $CsSnCl_3$ (1.52 eV) under idealized, defect-minimized conditions (bulk defect density 10^{16} cm^{-3}, zero interface defects). Experimentally synthesized $CsSnCl_3$ exhibits a bandgap of ~2.8 eV, and realistic defect densities (10^{16}–10^{17} cm^{-3} bulk, 10^{10}–10^{11} cm^{-2} interface) would reduce PCE to approximately 15–22%. Therefore, this study provides design guidelines for future bandgap engineering efforts rather than predictions of currently achievable experimental performance.

Declaration of generative AI usage

During the preparation of this work, the authors used Grammarly and ChatGPT for language polishing, grammar correction, and readability improvement. The authors reviewed and edited all content generated or suggested by these tools and take full responsibility for the final publication.

CRediT authorship contribution statement

Ghodrat Mahmoudi: Validation, Methodology, Conceptualization, Supervision, Writing – review & editing. **Masood Mehrabian:** Writing – original draft, Visualization, Software, Methodology, Formal analysis, Conceptualization. **Pourya Norouzzadeh:** Data curation, Formal analysis, Software, Validation, Writing – review & editing. **Maryam Taleb-Abbasi:** Writing – original draft, Data curation, Formal analysis, Investigation. **Asmet N. Azizova:** Resources, Validation, Writing – review & editing. **Sonya Aslyousefzadeh:** Visualization, Formal analysis, Investigation. **Omid Akhavan:** Writing – review & editing, Supervision, Project administration, Methodology, Conceptualization, Funding acquisition.

Declaration of competing interest

The authors declare that they have no known competing financial interests or personal relationships that could have appeared to influence the work reported in this paper.

Supplementary materials

Supplementary material associated with this article can be found, in the online version, at doi:10.1016/j.rineng.2026.111507.

Data availability

The SCAPS-1D input files (including layer parameters, defect densities, thicknesses, and simulation settings) and the generated output data (current-voltage characteristics, external quantum efficiency spectra, impedance spectra, and capacitance-voltage data) supporting this study are available from the corresponding author (Omid Akhavan, oakhavan@sharif.edu) upon reasonable request. The data are not pub-

licly archived due to the large number of simulation files and the specific formatting required by SCAPS-1D.

References

[1] J. Tong, C. Dong, M. Yao, Q. Wang, C. Shen, Y. Yue, L. Yan, Y. Gao, G. Yue, W. Zhang, 22.1% Carbon-electrode perovskite solar cells by spontaneous passivation and self-assembly of hole-transport bilayer, ACS Nano 19 (2025) 12960–12970, https://doi.org/10.1021/acsnano.4c16916.

[2] A. Mahapatra, D. Prochowicz, M.M. Tavakoli, S. Trivedi, P. Kumar, P. Yadav, A review of aspects of additive engineering in perovskite solar cells, J. Mater. Chem. A 8 (2020) 27–54, https://doi.org/10.1039/C9TA07657C.

[3] M. Kar, R. Sarkar, S. Pal, P. Sarkar, Lead free two-dimensional mixed tin and germanium halide perovskites for photovoltaic applications, J. Phys. Chem. C 125 (2020) 74–81, https://doi.org/10.1021/acs.jpcc.0c08164.

[4] M. Mehrabian, O. Akhavan, N. Rabiee, E.N. Afshar, E.N. Zare, Lead-free MAGeI3 as a suitable alternative for MAPbI3 in nanostructured perovskite solar cells: a simulation study, Environ. Sci. Pollut. Res. 30 (2023) 57032–57040, https://doi.org/10.1007/s11356-023-26497-1.

[5] S. Ramawat, S. Kukreti, D.J. Sapkota, A. Dixit, Insight into the microband offset and charge transport layer's suitability for an efficient inverted perovskite solar cell: a Case study for tin-based B-γ-CsSnI3, Energy Fuels 38 (2024) 9011–9026, https://doi.org/10.1021/acs.energyfuels.4c00763.

[6] M. Mehrabian, M. Taleb-Abbasi, O. Akhavan, Using Cu2O/ZnO as two-dimensional hole/electron transport nanolayers in unleaded FASnI3 perovskite solar cells, Materials 17 (2024) 1064, https://doi.org/10.3390/ma17051064.

[7] J. Zhang, Y. Meng, A.-P. Wu, C. Jin, P.-X. Hou, W. Xu, D.I. Kutsarov, Z. Wu, D. Liu, Y. Shen, Integrating SWCNT to bridge the stability divide in scalable and manufacturable flexible perovskite solar modules, Joule (2025), https://doi.org/10.1016/j.joule.2025.102225.

[8] M.H. Rahman, F. Rayhan, O. Ghosh, A.E. Bajwa, M.S. Hosen, M.S. Uddin, M.A. Al Mashud, A. Kumer, M.M.H. Bappy, An in depth analysis of CsSnCl3 based perovskite solar cell with diverse ETLs and C6TBTAPH2 as HTL: a numerical analysis, J. Inorg. Organomet. Polym. Mater. (2025) 1–15, https://doi.org/10.1007/s10904-024-03452-2.

[9] M.K. Hossain, G.F.I. Toki, A. Kuddus, M.H.K. Rubel, M.M. Hossain, H. Bencherif, M. F. Rahman, M.R. Islam, M. Mushtaq, An extensive study on multiple ETL and HTL layers to design and simulation of high-performance lead-free CsSnCl3-based perovskite solar cells, Sci. Rep. 13 (2023) 2521, https://doi.org/10.1038/s41598-023-28506-2.

[10] M. Mehrabian, E.N. Afshar, O. Akhavan, TiO2 and C60 transport nanolayers in optimized Pb-free CH3NH3SnI3-based perovskite solar cells, Mater. Sci. Eng. B 287 (2023) 116146, https://doi.org/10.1016/j.mseb.2022.116146.

[11] R.D. Chavan, B. Bończak, J. Kruszynska, A. Mahapatra, M. Ans, J. Nawrocki, K. Nikiforow, P. Yadav, J. Paczesny, F. Sadegh, Molecular engineering of azahomofullerene-based electron transporting materials for efficient and stable perovskite solar cells, Chem. Mater. 35 (2023) 8309–8320, https://doi.org/10.1021/acs.chemmater.3c01995.

[12] R. Alabada, A. Kumar, N. Ulloa, B.V. Barahona, F. García, A. Makrariya, Efficiency and stability enhancement in FA-based perovskite solar cells using controlled reduction of graphene oxide interlayer–an experimental investigation, Synth. Met. 304 (2024) 117578, https://doi.org/10.1016/j.synthmet.2024.117578.

[13] R. Sinha, A theoretical study on the insights of designing and optimization of a CsSn (IxBr1-x) 3 based solar cell, Renew. Energy 237 (2024) 121852, https://doi.org/10.1016/j.renene.2024.121852.

[14] Q. Fatima, A.A. Haidry, R. Hussain, H. Zhang, Device simulation of a thin-layer CsSnI3-based solar cell with enhanced 31.09% efficiency, Energy Fuels 37 (2023) 7411–7423, https://doi.org/10.1021/acs.energyfuels.3c00645.

[15] B.R. Hunde, A.D. Woldeyohannes, Performance analysis and optimization of perovskite solar cell using SCAPS-1D and genetic algorithm, Mater. Today Commun. 34 (2023) 105420, https://doi.org/10.1016/j.mtcomm.2023.105420.

[16] J.L. Surel, P. Caprioglio, J.A. Smith, A. Dasgupta, F. Furlan, C. Henderson, F. Yang, B.M. Gallant, S. Seo, A. Knight, Approaching the radiative limits for wide bandgap perovskite solar cells using fullerene blend electron transport interlayers, EES Sol. 1 (2025) 567–579, https://doi.org/10.1039/D5EL00103J.

[17] M. Mehrabian, P. Norouzzadeh, R. Yahyabonyad, A.N. Azizova, O. Akhavan, Built-in potential engineering via C60 buffer layer for high-performance CsSnGeI3 QD/CsSnBr3 hybrid perovskite solar cells, J. Phys. Chem. Solids (2025) 113259, https://doi.org/10.1016/j.jpcs.2025.113259.

[18] U. Asghar, M.A. Qamar, O. Hakami, S.K. Ali, M. Imran, A. Farhan, H. Parveen, M. Sharma, Recent advances in carbon nanotube utilization in perovskite solar cells: a review, Micromachines 15 (2024) 529, https://doi.org/10.3390/mi15040529.

[19] D.V. Krasnikov, H.A. Butt, V.A. Dmitrieva, S.I. Serebrennikova, O.R. Trepalin, A. R. Vildanova, V.A. Kondrashov, A.E. Goldt, D.V. Dzhurinskiy, J.A. Baimova, Ethylene-induced welding of single-walled carbon nanotube films to enhance mechanical and optoelectronic properties, Carbon 238 (2025) 120230, https://doi.org/10.1016/j.carbon.2025.120230.

[20] M. Khosrozadeh, K. Mabhouti, P. Norouzzadeh, R. Naderali, Complex impedance spectroscopy, dielectric response, and magnetic properties of the La0. 7 Sr0. 3BO3 (B= Mn, Fe, Co, or Ni) perovskite oxides, Ceram. Int. 50 (2024) 315–328, https://doi.org/10.1016/j.ceramint.2023.10.105.

[21] I. Matacena, P. Guerriero, L. Lancellotti, B. Alfano, A. De Maria, V. La Ferrara, L. V. Mercaldo, M.L. Miglietta, T. Polichetti, G. Rametta, Impedance spectroscopy analysis of perovskite solar cell stability, Energies 16 (2023) 4951, https://doi.org/10.3390/en16134951.

[22] E. Von Hauff, D. Klotz, Impedance spectroscopy for perovskite solar cells: characterisation, analysis, and diagnosis, J. Mater. Chem. C 10 (2022) 742–761, https://doi.org/10.1039/D1TC04727B.

[23] I. Matacena, L. Lancellotti, S. Daliento, B. Alfano, A. De Maria, V. La Ferrara, L. V. Mercaldo, M.L. Miglietta, T. Polichetti, G. Rametta, Impedance spectroscopy of perovskite solar cells with SnO 2 embedding graphene nanoplatelets, IEEE J. Photovolt. 13 (2023) 866–872, https://doi.org/10.1109/JPHOTOV.2023.3301674.

[24] J. Wagner, R.D. Chavan, J. Kruszynska, M. Ans, A. Mahapatra, N. Mrkyvkova, P. Siffalovic, P. Yadav, M. Ebic, S. Akin, T-shaped-N-doped polycyclic aromatic hydrocarbons: a new concept of dopant-free organic hole-transporting materials for perovskite solar cells, ACS Appl. Mater. Interfaces 16 (2024) 64940–64950, https://doi.org/10.1021/acsami.4c18636.

[25] M. Ans, Z. Biyiklioglu, A. Mahapatra, R.D. Chavan, J. Kruszyńska, M. Unal, H. Fazlı, K. Nikiforow, P. Yadav, S. Akin, Revealing the impact of aging on perovskite solar cells employing nickel phthalocyanine-based hole transporting material, Adv. Sci. 11 (2024) 2405284, https://doi.org/10.1002/advs.202405284.

[26] S.V. Pandey, D. Prochowicz, A. Mahapatra, S. Pandiaraj, A. Alodhayb, S. Akin, P. Yadav, The circuitry landscape of perovskite solar cells: an in-depth analysis, J. Energy Chem. 94 (2024) 393–413, https://doi.org/10.1016/j.jechem.2024.02.041.

[27] M.K.A. Mohammed, A.K. Al-Mousoi, S.M. Majeed, S. Singh, A. Kumar, R. Pandey, J. Madan, D.S. Ahmed, D. Dastan, Stable hole-transporting material-free perovskite solar cells with efficiency exceeding 14% via the introduction of a malonic acid additive for a perovskite precursor, Energy Fuels 36 (2022) 13187–13194, https://doi.org/10.1021/acs.energyfuels.2c02878.

[28] R.D.C. Yukta, A. Mahapatra, D. Prochowicz, P. Yadav, P.K. Iyer, S. Satapathi, Improved efficiency and stability in 1, 5-diaminonaphthalene iodide-passivated 2D/3D perovskite solar cells, ACS Appl. Mater. Interfaces 15 (2023) 53351–53361, https://doi.org/10.1021/acsami.3c09887.

[29] M.K. Hossain, G.F. Ishraque Toki, D.P. Samajdar, M.H.K. Rubel, M. Mushtaq, M. R. Islam, M.F. Rahman, S. Bhattarai, H. Bencherif, M.K.A. Mohammed, Photovoltaic performance investigation of Cs3Bi2I9-based perovskite solar cells with various charge transport channels using DFT and SCAPS-1D frameworks, Energy Fuels 37 (2023) 7380–7400, https://doi.org/10.1021/acs.energyfuels.3c00540.

[30] M. Mehrabian, M. Taleb-Abbasi, O. Akhavan, Effects of electron transport layer type on the performance of Pb-free Cs2AgBiBr6 double perovskites: a SCAPS-1D solar simulator–based study, Environ. Sci. Pollut. Res. 30 (2023) 118754–118763, https://doi.org/10.1007/s11356-023-30732-0.

[31] M. Burgelman, P. Nollet, S. Degrave, Modelling polycrystalline semiconductor solar cells, Thin Solid Films 361 (2000) 527–532, https://doi.org/10.1016/S0040-6090(99)00825-1.

[32] M. Burgelman, J. Marlein, Analysis of graded band gap solar cells with SCAPS, in: Proc. 23rd Eur. Photovolt. Sol. Energy Conf. Val., Citeseer, 2008, pp. 2151–2155, https://doi.org/10.4229/23RDEUPVSEC2008-3DO.5.2.

[33] M. Burgelman, J. Verschraegen, S. Degrave, P. Nollet, Modeling thin-film PV devices, Prog. Photovolt. Res. Appl. 12 (2004) 143–153, https://doi.org/10.1002/pip.524.

[34] S.S. Urmi, M.A.K. Khan, T.T. Ferdous, D. Adinehloo, V. Perebeinos, M.A. Alim, Cs2TiI6 (Cs2TiIxBr6-x) Halide perovskite solar cell and its point defect analysis, Nanomaterials 13 (2023) 2100, https://doi.org/10.3390/nano13142100.

[35] M. Baro, P. Borgohain, SCAPS-1D device simulation of highly efficient perovskite solar cells using diverse charge transport layers, J. Electron. Mater. 52 (2023) 7623–7644, https://doi.org/10.1007/s11664-023-10681-7.

[36] V. Bhojak, P.K. Jain, Theoretical analysis of power conversion efficiency of lead-free double-perovskite Cs2TiBr6 solar cells with different hole transport layers, Engineering 6 (2025) 28, https://doi.org/10.3390/eng6020028.

[37] G. Xosrovashvili, N.E. Gorji, Numerical simulation of carbon nanotubes/GaAs hybrid PV devices with AMPS-1D, Int. J. Photoenergy 2014 (2014) 784857, https://doi.org/10.1155/2014/784857.

[38] P.L. McEuen, J.-Y. Park, Electron transport in single-walled carbon nanotubes, MRS Bull. 29 (2004) 272–275, https://doi.org/10.1557/mrs2004.79.

[39] P. Avouris, J. Appenzeller, R. Martel, S.J. Wind, Carbon nanotube electronics, in: Proc. IEEE 91, 2004, pp. 1772–1784, https://doi.org/10.1109/JPROC.2003.818338.

[40] T. Dürkop, S.A. Getty, E. Cobas, M.S. Fuhrer, Extraordinary mobility in semiconducting carbon nanotubes, Nano Lett. 4 (2004) 35–39, https://doi.org/10.1021/nl034841q.

[41] M. Ourabi, S. Garg, B. Mirka, R. Ewenike, M.N. Tousignant, M. Ranne, A. Adronov, B.H. Lessard, Networks of conjugated polymer-wrapped single-walled carbon nanotubes through controlled drop-dispensing for thin-film transistors, ACS Appl. Nano Mater. 6 (2023) 11242–11251, https://doi.org/10.1021/acsanm.3c01265.

[42] P. Lamberti, S.A. Mousavi, G. Spinelli, V. Tucci, V. Wagner, Fabrication and charge transport modeling of thin-film transistor based on carbon nanotubes network, IEEE Trans. Nanotechnol. 13 (2014) 795–804, https://doi.org/10.1109/TNANO.2014.2322284.

[43] O. Saidani, A. Yousfi, D.P. Samajdar, X. Xu, T.B. Zemene, S. Bhattarai, M. K. Hossain, G.S. Sahoo, Revealing the secrets of high performance lead-free CsSnCl3 based perovskite solar cell: a dive into DFT and SCAPS-1D numerical insights, Sol. Energy Mater. Sol. Cells 277 (2024) 113122, https://doi.org/10.1016/j.solmat.2024.113122.

[44] M.K. Hossain, G.F.I. Toki, A. Kuddus, M.K.A. Mohammed, R. Pandey, J. Madan, S. Bhattarai, M.F. Rahman, D.K. Dwivedi, M. Amami, Optimization of the

architecture of lead-free CsSnCl3-perovskite solar cells for enhancement of efficiency: a combination of SCAPS-1D and wxAMPS study, Mater. Chem. Phys. 308 (2023) 128281, https://doi.org/10.1016/j.matchemphys.2023.128281.
[45] P. Jadeja, S. Yadav, A. Ravalia, S. Katba, Investigating the impact of various electron transport layers on the performance of Sn-based perovskite Solar cells: a device simulation using SCAPS-1D, J. Phys. Chem. Solids (2025) 113088, https://doi.org/10.1016/j.jpcs.2025.113088.
[46] M.T. Alemu, D.F. Hirpa, K.O. Obodo, C.A. Geffe, Computational investigation of antimony-doped CsSnCl3 halide perovskites: insights into structural, electronic, optical, and photovoltaic performance analysis, Comput. Condens. Matter. 43 (2025) e01045, https://doi.org/10.1016/j.cocom.2025.e01045.
[47] F. Karim, M.H.R. Aslam, A.I. Suva, High-efficiency lead-free CH3NH3SnI3 perovskite solar cell with inorganic transport layers: SCAPS-1D and PVSyst-based numerical study, J. Phys. Chem. Solids (2025) 113175, https://doi.org/10.1016/j.jpcs.2025.113175.
[48] H. Rajasekaran, T. Vasudevan, L.-C. Chen, Numerical investigation of high-performance bilayer tin-based perovskite solar cells with SCAPS-1D, Mater. Adv. (2026), https://doi.org/10.1039/D5MA01437A.
[49] J.Y. Jiang, Solar cell efficiency tables (Version 66), Prog. Photovolt. Res. Appl. 33 (2025) 795–810, https://doi.org/10.1002/pip.3919.
[50] F. Izadi, A. Ghobadi, A. Gharaati, M. Minbashi, A. Hajjiah, Effect of interface defects on high efficient perovskite solar cells, Optik 227 (2021) 166061, https://doi.org/10.1016/j.ijleo.2020.166061.
[51] D.I. Amune, W. Fidel, R.K. Koech, D. Sanni, J. Botsoa, V. Anye, E. Nstoenzok, Enhancing stability and efficiency in perovskite solar cells: insights into inorganic HTL deposition and interface defect passivation, Energy Adv. (2026), https://doi.org/10.1039/D5YA00353A.